3-D digital outcrop model for analysis of brittle deformation and lithological mapping (Lorette cave, Belgium)

A. Triantafyllou, A. Watlet, Stéphane Le Mouélic, T. Camelbeeck, F. Civet, O. Kaufmann, Y. Quinif, S. Vandycke

3-D Digital Outcrop Model for analysis of brittle deformation and lithological mapping (Lorette cave, Belgium)

A. Triantafyllou, A. Watlet, S. Le Mouélic,
T. Camelbeeck, F. Civet, O. Kaufmann, Y. Quinif, S. Vandycke

1. Introduction

High-resolution Digital Outcrop Models (DOMs) are becoming increasingly attractive tools for modern field geologists. Such 3D models already show widespread applications across the geosciences, such as the characterization of inaccessible geological structures (e.g., Smith et al., 2016; Chesley et al., 2017; Vollgger and Cruden, 2016; Assali et al., 2014; Corradetti et al., 2018), the investigation of geomorphological processes (e.g., Fonstad et al., 2013; Micheletti et al., 2015a), or the assessment of natural resources and geohazard (e.g., Abellan et al., 2016; Esposito et al., 2017). Specifically, for structural geology purposes, DOMs are of great interest because they can provide a continuous spatial observation in terms of rock units, lithological contacts and geometries of geological structures. Such novel kind of datasets represent significant inputs for new quantitative structural modelling and may bring new clues with respect to traditional sectional interpretations (Bistacchi et al., 2011; Chalke et al., 2012; Franceschi et al. 2015).

Three main methods are commonly used for acquiring 3D datasets: *(i)* tacheometric surveying instruments (i.e. traverse via distance meters, compasses, tilt meters or total stations), *(ii)* terrestrial laser/light-based scans (LIDAR) and *(iii)* digital photogrammetry technology using photographs captured from the ground using field digital camera and/or from an Unmanned Aerial Vehicle (UAV) (Lerma et al., 2010; Westoby et al., 2012). The first method requires intensive acquisition works and complex data processing resulting in low spatial-resolution data sets (Gallay et al., 2015). Conversely, the two other methods offer a higher resolution acquisition of the outcrop. Both of these methods have their own advantages and limitations, thoroughly discussed by Baltsavias (1999), Remondino et al. (2011) and Wilkinson et al. (2016). Terrestrial Laser Scanning systems (TLS) are able to create high resolution and high precision 3D point clouds, but such methods are generally costly, especially for sporadic surveys (e.g., Wilkinson et al., 2016; Oludare Idrees and Pradhan, 2016). Compared to laser-based methods, digital photogrammetry is generally a cheaper method. In addition, digital cameras needed to capture raw data, are lightweight and can be embedded on mobile and/or remote shooting systems (e.g., poles, cables, unmanned aerial vehicles). This approach provides more flexibility to use digital photogrammetry in various types of environments. It also has the advantage to capture a 3-channel (r, g, b)

spectral information in addition to the topographical data. The considerable use of digital photogrammetry this last decade is also due to the rise of many affordable software packages producing DOMs (e.g., Agisoft Photoscan, MicMac, VisualSFM; Niederheiser et al., 2016) as well as the democratization of personal computers with high RAM memory capacity and ultra-fast central and graphic processor units.

Cave systems stand out as exceptional environments for studying sedimentary and tectonic structures because of their generally better preservation from atmospheric erosion processes than for surface outcrops. However, mapping and modelling their complex geometries may be a challenging task due to limited accessibility and light conditions. Although geological structures are numerous and easy to identify, quantifying their orientation may be complicated or impractical due to their inaccessibility. In addition, such structural records may also be difficult to integrate in a regional tectonic scheme because of a lack of underground geographic reference. In such environments, building DOMs with digital photogrammetry sounds challenging. This approach has already been used for the preservation of archaeological heritage (Lerma et al., 2010) but is still poorly used for geoscientific purposes despite the great source of information that it may provide. Indeed, high resolution 3D surface models of cave chambers may provide spatialized data to produce precise morphological maps and conduct volumetric analyses (e.g., Roncat et al., 2011; Zlot and Bosse, 2014). Such data could also complement studies of active- or paleo-seismicity and their relations with collapse structures, speleothem damages and absolute dating of karstification processes (e.g., Sebela et al., 2005; Camelbeeck et al., 2012, Margielewski and Urban, 2017; Salomon et al., 2018). In karst systems, constraining geometries of planar discontinuities (*i.e.* faults, bedding planes, etc.) and localizing specific types of lithology in 3D are also crucial aspects for investigating hydrological processes and more specifically groundwater infiltration (e.g., Jaillet et al., 2011; Mahmud et al., 2016; Watlet et al., 2018).

In these perspectives, we present here a challenging study conducted in one of the main chamber (ca. 10 000 m^3) of the Lorette cave (Rochefort, South Belgium). Its roof exhibits an important sedimentary pile that recorded Variscan to recent active brittle tectonics being inaccessible for direct measurements of geological structures. The aims of this research paper is to present a workflow for *(i)* acquiring data and building a Digital Outcrop Model of a lowlight and geometrically complex cave site using digital photogrammetry, *(ii)* georeferencing the 3D model in an underground environment, *(iii)* characterizing the geometry of inaccessible geological structures and their tectonic kinematics (e.g., faults, joints, sedimentary beds) and *in fine*, *(iv)* comparing them to accessible structures measured in the field and integrate them into the regional geodynamics. In this paper, the orientation of

planar structures will be reported in full strike-dip notation and those of linear structure in full trend-plunge.

2. Geological framework

The study site is part of the Rochefort Cave Laboratory (Quinif et al., 1997) located in the central part of the Lorette cave, close to the city of Rochefort (southern Belgium; Fig. 1a). It belongs to an extended karstic network developed in Devonian and Carboniferous limestone of the Ardennes massif, forming some of the largest caving systems of Belgium (Willems and Ek, 2011). This massif has been intensively folded, faulted and thrusted during Variscan orogenesis (Fig. 1 a-b; Michot, 1980; Pirson et al, 2008) forming successive folds interspersed by faulted structures striking ENE. In this framework, the Lorette cave is situated in Givetian limestone, in the inverse flank of an overturned fold (Fig. 1 a-b), in inverse stratigraphic series striking N070 and dipping 55°SSE (Marion et al., 2011). They are composed of series of decimetric series of massive limestone interspersed with porous/weathered limestone strata and occasional thin clay interbeds (Marion et al., 2011). The Lorette cave itself is composed of a well-developed subsurface network (Quinif et al., 1997; Camelbeeck et al., 2011) made of tunnels with diameters of several meters along strike crosscut by smaller passages developed along the dip of the stratigraphic units. At the surface of this area, a large sinkhole gives access to the Lorette cave, which opens onto a large chamber, called the Val d'Enfer chamber, the case study of this paper (Fig. 1c). This one connects with small passages to the north (Fig. 1c). The Val d'Enfer chamber is thought to be formed via massive collapses of which two scree slopes on the sides of the cavity are the relics (Willems and Ek, 2011; Quinif et al. 2011). Several limestone layers are exposed along the walls and roof of the room. This part of Lorette Cave stands between 180 and 190 m AOD (Above Ordnance Datum; i.e. height relative to the average sea level), corresponding to 40 to 30 meters below the topographical surface. Two episodes of faulting have been recognized in the Lorette cave. A first episode has been described in Vandycke and Quinif (2001; Fig. 1b) as reverse motion along the bedding planes which is attributed to Variscan tectonics. The second faulting episode is proven to be active posterior to the karstogenesis. These active faults are expressed as reactivated bedding planes with a normal displacement marked by thin argillaceous bearing slickensides (Camelbeeck et al., 2011).

3. Field survey and data acquisition

3.1 Field digital cameras and cave lighting

For the applicability of the photogrammetric survey, pictures of the outcrop must be taken from a sufficient amount of singular points of view. The goal of the survey is to get an image of each part of the chamber internal surface from multiple points of view. For that purpose, we combined photographs from two different devices: one digital camera taking pictures from the ground and a digital camera embedded on an Unmanned Aerial Vehicles (UAV, i.e. remotely piloted aircraft). In this study, the DJI Phantom 3 Pro multi-rotors vehicle was used in order to operate in confined environments in fully manual flight mode. This drone is equipped with three lithium polymer (LiPo) battery each of which give an autonomy of approximately 20 min. The field camera consists of a Nikon D5300 (23.5 x 15.6 mm CMOS sensor; photographs size of 6000 x 4000 pixels) with a fixed 18mm lens (2.8 of focal ratio) and the UAV default action camera (50.8 x 25.4 mm CMOS sensor; photographs size of 4000 x 3000 pixels) with a fixed 35mm lens (2.8 of focal ratio). For more post-production flexibility, all pictures from each digital camera were captured as RAW data files (equivalent of 'digital negatives' recording all the data captured by the sensor without white balance set, etc.). During field operations, we ensured, as far as possible, an image overlap of 60% – 85% (as recommended by Agisoft LLC, 2015). Overall, using these two cameras reduces the acquisition time and tends to enhance the resolution of the produced 3D model. Data sets of 1090 and 215 photographs were taken with the Nikon and the DJI digital camera in total. Capture parameters were adapted for both sensors (mean ISO: 5970 - 898; mean aperture: 3.6 - 2.8 and mean shutter speed: 1/43 - 1/6 second for Nikon DSLR - DJI digital camera, respectively).

Another mandatory condition concerns the lighting of the outcrop of interest. This one must benefit an optimum illumination avoiding shadows and over-exposure which in both cases, can result in a loss of pixel information. For that purpose, we equipped with 2 x 1000 Watts and 4 x 500 Watts halogen spotlights (with 3000K light temperature). Given to the size of the Val d'Enfer chamber, we proceeded to six successive surveys/partial lighting of the room (Fig. 2 a-b). Each portion of the room was illuminated by setting the spotlights along a semi-circle line covering and pointing towards the outcrop of interest. We managed this subdivision to ensure sufficient overlap between each surveyed zone (Fig. 2a).

3.2 Ground Control Points (GCP) and Ground Control Tri-axes (GCT).

Several Ground Control Points (GCP) were positioned within the Val d'Enfer chamber (Fig. 2a). They are marked by large steel nails hammered in stable rocks and precisely positioned in absolute space (XYZ in Belgian Lambert 72, from a previous study; Watlet, 2017) using a DGPS station (Altus APS-3 rover connected to the Walcors GPS network from the Public Service of Wallonia; Walcors, 2016) at the surface. These GCP are spread from the entrance

doline of the Lorette cave to the Val d'Enfer chamber and cover the entire subsurface network of the cave (Fig. 2a). These GCP points will be used to translate the model in local geographic coordinates (*cf.* section 4.3). In addition, two Ground Control Tri-axes (GCT; Fig. 2c) were placed at the western and eastern sides of the Val d'Enfer chamber (see. Fig. 2a). Each GCT is made of three boards (precisely 0.1 m wide and 1 m long) pointing to three directions orthogonal to each other (see Fig. 2c). Each board is colored with a specific bright flashy colour (red, yellow and green) that is not found elsewhere in the room. The red, yellow and green boards are installed orthogonally to each other with the two latter being ground-levelled and the yellow board precisely pointing to the north in which the orientation was calibrated with a field and a digital compass. The base of the western GCT is positioned on the GCP50 (Table A1 in the appendices). Both GCT will be used to level the digital outcrop model, reorient it according to the north and finally, in order to test and validate the proportions of the georeferenced model (see section 4.3 below). The absolute distance between GCP50 and the stainless spike GCP58 was also measured using a laser-based distance-meter (Leica 790656 Disto X310; ±1 mm precision).

4. Building and georeferencing the DOM of the Val d'Enfer chamber

Digital photogrammetry was used for the reconstruction of the digital outcrop model of the Val d'Enfer chamber. This approach uses the apparent displacement of the position of a feature to model with respect to a reference point (called the parallax), itself caused by a shift in the point of view (here, the location of the camera; Allum, 1966). This principle has been implemented in digital photogrammetry software via the Structure-from-Motion (SfM) algorithm which allows to compute the geometry of an object to model using the parallax. This method is thoroughly explained and reviewed in several papers describing the optical principle itself (e.g., Micheletti et al., 2015b; Carrivick et al., 2016) as well as its implementation in numerous software (e.g., Niederheiser et al., 2016). This section goes through the initial steps before extracting exploitable results, including the pre-processing of the raw photographs, the reconstruction of the point cloud by SfM photogrammetry, triangulation and building of a mesh and finally, the georeferencing of the digital model. This workflow is detailed in the Figure 4.

4.1 Pre-processing of individual photographs.

The outcrops in the Val d'Enfer cave chamber is made of complex and irregular concave/convex shapes. Such geometry can lead to physical occlusion of some portions of the outcrop, shadows and over-exposure caused by directional artificial lightings (Fig. 3). The presence of shadows/overexposed zones may however form poorly reconstructed parts of

the final model (low density of tie points) and such variation of exposure can also be problematic for further model-based interpretations of the lithology. The resulting dark or light colours may indeed not be representative of the lithology at the surface. This could lead to misinterpretations between dark rock surface and/or in shadowed zones. Blurry photographs were removed using a routine python script and a home-made Photoshop script was used to correct over-exposure. This consists of correcting each RAW photograph by darkening the overexposed zones and by lightening the shadowed portions of the photographs as well as adjusting the white balance to correct halogen 3000K yellowish colours (Fig. 3). After this treatment, each picture was automatically converted and saved as a JPG image file type.

4.2 Building the 3D dense point cloud and mesh using SfM photogrammetry.

In order to build the digital outcrop model of the Val d'Enfer chamber, enhanced photographs are imported and processed using Agisoft Photoscan Pro software v. 1.3.4 (see Appendix B1 for used parameters in Agisoft Photoscan software and desktop computer specifications). The EXIF metadata of each image (EXIF, 2012) including the focal length and the pixel size are automatically read by the software when importing the photographs. These metadata are used to calibrate the inner parameters of each camera (internal and external camera orientation parameters, distortion coefficients, etc.). The camera locations and a sparse point cloud are then computed in generic mode. This mode allows faster processing of big amount of non-geotagged photographs finding overlapping images using downscaled copies of original images and then, refining the computation of tie points locations progressively using higher resolution images (Agisoft LLC, 2015). This first step results in a sparse point cloud made of 1.2 million points (Fig. 4a). In this point cloud, some outliers are identified. We manually reset the alignment of the pictures in which these tie points are identified, to correct for such erroneous point positions. In case of no improvements, these outliers are manually removed from the sparse point cloud. Based on this first dataset, a high resolution dense point cloud is computed, which results in 395.4 million points, providing a point density of approximately 1.65 million points per square meters (Fig. 4b). Some small and localized holes occur in the point cloud, especially in small complex-geometry areas (e.g., narrow corridors) which obstruct the lighting system or the camera view.

Building a mesh model from such a huge dataset requires massive computation resources in terms of RAM- and GPU-memory (Agisoft LLC, 2015). Therefore, the point cloud has been splitted in 11 chunks to facilitate the processing workflow. Individual meshes were successfully computed for each chunk and then merged into a single high-resolution 3D mesh, made of 40.2 million of polygons (ca. 18 600 polygons/m², Fig. 4 c-d). Compared to the point cloud model, the mesh consists of a digital surface model of the outcrop allowing to

provide volumetric estimation and topological information of the cave. This is also a crucial step before creating a model texture. These further steps allow to minimize the size of the digital model and computation resources needed to render and visualize it, which is mandatory in order to share it via 3D platforms and/or virtual reality technologies (Remondino, 2011; Triantafyllou et al., 2018) but those are beyond the scope of this paper. In this study, we focus on the dense point cloud which is finally exported in an ASCII text file for further processing in CloudCompare software (see next section). Every point is characterized by 9 attributes: the relative location (x, y, z coordinates), the colour calculated from the original pictures (red, green, blue channels ranging from 0 to 255) and orientations of the normal vectors (nx, ny, nz ranging from -1 to 1). The latter are computed along with the dense point cloud in Agisoft software. They provide a geometrical information for each point and consist of the normal vector of a local surface delimited by the nearest neighbours of each specific point (Agisoft LLC, 2015). A textured low resolution version of the 3D model of the main chamber of the Lorette cave has been uploaded on the sketchfab open repository and can be accessed online through this link: *https://skfb.ly/6FQNw* .

4.3 Georeferencing the Digital Outcrop Model

The resulting high-resolution 3D points cloud needs to be levelled, oriented according to the north, scaled and translated to geographical coordinates for facilitating regional geology interpretations (Fig. 4 e-f). We used the location and orientation of GCP and GCT references along with CloudCompare software version 2.9 (Girardeau-Montaut, 2015) combined with our own Python routines specifically developed for this study. Firstly, the DOM, arbitrarily oriented when outputting from Agisoft software, is levelled. Points colored in flashy green and yellow (forming the Ground Control Triaxes; GCT, see section 3.2) are detected and extracted from the point cloud. The polar median of their normal vectors is calculated and compared to an expected upward vertical vector [0, 0, 1]. We retrieve the corresponding transformation matrix and apply it to the entire digital model. Secondly, the levelled model is rotated along the Z axis only, superimposing the direction pointed by the length of the yellow board (pointing to the magnetic north; plus, correcting from the magnetic declination to point to the geographical north) and the Y direction of the reference model axis (pointing to the virtual north; Fig. 4f). Thirdly, the distance between the GCT and Ground Control Points (GCPs; Table A1) is used to scale the digital model. Relative distances are measured in the field using a laser-beam distance-meter (Leica 790656 Disto X310), showing for example an absolute distance of 35.60 m (± 1 mm) between the basis of the western tri-axis (GCP50) and the GCP58 reference spike. The ratio between this real value and the modelled distance is applied as a scaling factor to all dimensions of the digital outcrop model, while preventing

at this point any model's rotation. The relative scaling error is of 0.0028% (*i.e.* less than 2 mm error for the 3D project extension). In order to position the model in the projected coordinates Belgian Lambert 72 (EPSG:31370), the levelled, oriented and scaled model is finally translated in X, Y and Z to absolute geographical coordinates using the GCP50 station (in meters, X= 211303.20, Y = 94111.41 and Z = 178.06).

In order to validate the referencing and proportions of the digital outcrop model, we measured the length size of the western and eastern GCT boards. The length of each 1-meter-long board (green and yellow ones) was measured in CloudCompare along six parallel sections covering the 0.1 m width of the board. These data are shown in the Table 2 in the Appendix A2 and are comprised between 0.99 m and 1.03 meter with a median of 1.01 m. This two-location test also attests that the digital model is well proportioned in all dimensions. These results are in agreement with those of Watlet (2017) in the same Val d'Enfer chamber. This author provided a comparison of the point clouds acquired with a LiDAR survey and the digital model from this study computed by Sfm photogrammetry, highlighting the excellent proximity between most of the points from both models. The M3C2 method developed by Lague et al. (2013) allowed to compute distances between the two scaled point clouds (using here the LIDAR point cloud as reference) which showed that both point clouds match within a standard deviation of 0.03 m.

5. From DOM to geological interpretations

When the digital outcrop model is correctly georeferenced, oriented and sized, it can be used to efficiently extract lithological and structural informations: in particular, for constraining the geometry of discontinuities (e.g., faults, joints and sedimentary bedding planes). As shown in previous sections, the high density of points of the 3D model (1.65 M points/m^2) is sufficient to carry out the work of points extraction. This represents a crucial source of information to get a better understanding of the local water infiltration, past- or present tectonic activity. Such 'virtual survey' is conducted combining manual and semi-automatic data extraction for further geological interpretations, similarly to a traditional field survey while covering portions of the outcrop inaccessible to the fieldworker.

5.1 Extracting a detailed morphological map and lithostratigraphic log

The DOM of the Val d'Enfer chamber provides an exhaustive sample of the sedimentary pile exposed in this part of the karstic system. Based on our field survey and previous studies in the Lorette cave (Quinif et al., 2011 and references therein), we know that exposed lithologies mainly consist of carbonate mudstones alternating with thin clay interbeds. A

detailed field survey of accessible bedding layers from both types of lithology (Fig. 5 a-b) made possible to identify that layers that display dark hues are characterized by higher clay contents, whereas lighter colours (mid to light grey; Fig. 5b) correspond to more calcitic limestone layers.

Three 0.5-meter-wide parallel bands oriented normal to the striking direction of sedimentary bedding planes were extracted from the original point cloud. These bands have been chosen to be located where fresh rock outcrops, without colored traces of water runoff or superficial carbonates concretions. For each band, a slope map was produced, providing a colorized representation of the slope variation based on normals' data. This map allowed to precisely define the interface between bedding planes, typically associated with a high variation in slope; hence, corresponding to the top and bottom boundaries of each layer. The colour of each individual layer was averaged and finally classified/interpreted in terms of lithology as mudstone (mid- grey to light grey) or clay-rich mudstones (dark grey to black layers). Combining extracted data from each band of the DOM and field observations allowed to reconstruct a precise lithostratigraphic log of the sedimentary pile exposed on the roof and the walls of the Val d'Enfer chamber (Fig. 5a). Clayish limestone layers are important materials to detect in karstic environments as they may involve higher percolation discharge rates. Watlet et al. (2018) showed the importance of such a well constrained 3D model to interpret results from a hydrogeophysical monitoring of the epikarst. Indeed, the 3D information allowed to link the heterogeneity in lithological layers made of massive limestone and clayish limestone to variable dynamics of the local water infiltration.

The DOM also allows to create a detailed morphological map of the Val d'Enfer chamber (Fig. 9) showing a re-evaluation of the chamber extent (see comparison between Figures 2 and 9) and a more precise outline of collapse areas and their local variation of elevation. This study also allowed to map potential fault structures on the ground by extrapolating surveyed faults from the roof of the DOM.

5.2 Identifying and extracting the orientation of geological structures

We worked on four specific types of geological structures identified on the roof of the Val d'Enfer chamber, which are not directly accessible to the traditional compass. They consist of the aforementioned types of sedimentary bedding planes plus three kinds of brittle deformation structures, including fault planes (with their slickenlines and slickensides), joints and calcite filled veins (i.e. planar and sigmoidal *en-echelon* veins). Locating and identifying these structures through the DOM requires a back and forth observation approach between the original high resolution photographs of the roof of the Van d'Enfer chamber (Fig. 6 a-d) and the high density point cloud of the model itself. A thorough post-fieldwork survey allowed

to identify six fault planes with their kinematics, two subsets of calcitic veins and two subsets of joints. The orientation of planar structures is measured directly in CloudCompare using the virtual compass tool (Thiele et al., 2017; Fig. 7). Two main measurements methods have been used. (i) The first method consists of a direct measurement of the planar structure by averaging the normal vectors included in a virtual circle that delimits the region of interest (Fig. 7a). (ii) When the surface of a planar structure is not well exposed, a second tool allows to compute the best fitting plane based on the intersection trace between the plane of interest and the topography of the digital model (Fig. 7c). Both calculated normal vectors are finally converted in dip-direction values. Alternatively, linear data like slickenlines are measured by tracing a two-point line lying in the planar structure, using the same virtual compass toolbox in CloudCompare (Thiele et al., 2017; Fig. 7a). Table A3 summarizes the orientation of all the structures measured in the digital outcrop model.

5.2.1 Sedimentary bedding planes.

We measured the sedimentary bedding planes (n = 191 in total) in five subsets from the base (northward, A-bedding) to the top (southward, E-bedding) of lithostratigraphic pile in order to validate the monoclinic geometry of the sedimentary pile and/or track a potential variation of strata orientation due to high amplitude folded structures affecting the sedimentary units in the studied area. Detailed results are given in Table A3 and in the Fig. 5c. The median strike-direction value of the bedding planes is N065 with 48° dipping to the SE. The limited spread of the data supports that there is no significant variation of the orientation of the stratigraphic bedding through the sedimentary pile of the Val d'Enfer chamber (Fig. 5c). Two surfaces are marked by a stylolithic bedding surface. Indentation of the stylolites are normal to bedding suggesting they formed at an early stage during sediments compaction or compressional stress normal to the bedding planes.

5.2.2 Fault-slip data.

Based on their geometry, two groups of faults were identified in the roof of the Val d'Enfer chamber. Both fault planes are characterized by calcite filling that records the slip: (i) The main set of faults is south-dipping, with a relative offset along inherited bedding planes (F1, F2, F4 and F5; Fig. 8 b-c-e-f). This subset is characterized by a mean ENE strike and a moderate dip to the south (strike-dip polar median: N069-S42). Slickenlines were clearly identified in the 3D model and display a fault offset recorded by synchronous calcitic mineralization as well as in the massive carbonaceous rock. Their trends range between SSE to SE (trend polar median: N160 on the fault plane). Kinematics criteria may be challenging to determine despite clear asymmetric micro-scarps exposed on F2 and F5 faults (Fig. 8 d-g). Based on the morphology of the fault plane and direct observations made in the

field, these scarps show a reverse faulting movement (Fig. 6 a-b). Some minor argillaceous fillings have also been observed on the F5 fault plane (Fig. 6a) in which subparallel slickenlines are recorded but without clear kinematics argument due to their limited extents. Based on the nature of the filling and their geometry, it is clear that these tectonic markers correspond to the fault slip data measured in the same karstic system by Vandycke and Quinif, (2001), which is attributed to a recent reactivation of these faults (see next section). (ii) The second fault set is secant to the bedding planes and north-dipping (F3 and F6; Fig. 6 c-d). It is characterized by a E-W strike and a high dip to the north (strike-dip polar median: N279-N60). Slickenlines measured on these faults are very similar to those from the south-dipping fault planes as they also affect the massive core of the carbonaceous rock and are also underlined by *striae* supported by calcite fillings (Fig. 6). Their orientation is trending to the NW (trend-plunge polar median: N316/50). Kinematics criteria are more obvious here, marked by clear asymmetric micro-scarps at the surface of the fault plane. The light colour on these faults suggests that they form accretionary elongated calcite steps which also support a reverse sense of movement (Fig. 6d).

5.2.3 Calcite veins

Two sets of calcite veins were identified in the roof of the cave. Their respective orientations were measured using intersection traces with the roof topography in the digital outcrop model (Fig. 7 c-d). It includes: (i) planar calcite-filled veins that are strictly localized and delimited within sedimentary bedding (CJ1_A; n = 14). These veins form a WNW-striking planes with low-dips to the north (polar median at N285-N36; Fig. 8h). (ii) Sigmoidal calcite-filled veins marked by an en-echelon arrangement. These sigmoidal veins are very elongated and aligned, marking shear bands secant to the bedding planes (CJEch_A; n = 4). These bands were also measured using intersection traces with the roof topography of the DOM and are characterized by subhorizontal planes slightly dipping to the north (polar median strike-dip at N299-N24; Fig. 8i). These veins originate as tension gashes that are parallel to the major stress and fluid-assisted. Their sigmoidal en-echelon shape suggests that the central part of the vein has rotated while the calcitic vein was still lengthening during deformation, so that the sense of rotation indicates a normal sense of shear (top to the north).

6. Tectonic interpretations from virtually measured tectonic markers

We analysed brittle data measured in the digital model of the Van d'Enfer chamber (fault-slip, calcitic veins representing tension gashes, joints, etc.) in order to compare them to field measurements made in the Han-sur-Lesse region and eventually, use them for paleostress reconstruction. The similar strike direction between each brittle structure (fault, joint and

tension gashes) suggest they formed via a single progressive deformation event. This is also suggested by the nature, mainly calcitic, of the mineral infillings which developed during the formation of tension gashes and during faulting events. DOM observations suggest however that both sets of tension gashes formed prior to fracturation and faulting event. This is marked by a relative offset of these veins on both sides of faulted structures. The orientation of the principal stress axes can be derived from the distribution of extension veins that are assumed to form perpendicular to σ3 and align in the σ1 and σ2 plane. Accordingly, they can result from a compressional main axis oriented N-S and subhorizontal to slightly plunging to the north. One of the tension gash subset showing sigmoidal shapes (CJEch_A) indicates a sense of shearing top to north, in agreement with a N-directed vergence. Such syntectonic veins rotation and shearing has probably not been recorded by planar veins (CJ1_A) contained in single bedding layer due to the fact that shearing has been preferably accommodated at interbeds less competent layers like e.g. clayish bedding. Fault planes were also used for paleostress computation using the WinTensor software (Delvaux, 2011) and the procedure described in Delvaux and Sperner (2003) derived amongst others from Wallace (1951) and Angelier (1989, 1994). This stress inversion allows to reconstruct the 4 parameters of the tectonic stress tensor, including the orientation of the three orthogonal principal stress axes σ1, σ2, σ3, (where σ1 > σ2 > σ3) and the stress ratio Φ (σ2 - σ3) / (σ1 - σ3) (0 < Φ < 1) which expresses the magnitude of σ2 relative to the magnitudes of σ1 and σ3. These four parameters are first estimated with an improved version of the Right Dihedra method. For this purpose, we included faults for which the shear sense was confirmed by numerous reliable kinematic criteria surveyed on the DOM and in the field (see previous section), including F1, F2, F4, F5 faults as reverse bedding-plane slip probably reactivated as well as conjugated neoformed reverse faults (F3, F6). These results should not be compared to those from Vandycke and Quinif (2001) as they were working on active tectonics. Here, the calculated stress tensor is: σ1 (azimuth 326°/plunge 13°); σ2 (azimuth 233°/plunge 09°); σ3 (azimuth 110°/plunge 74°), Φ = 0.31. This system is characterized by a compressional main axis (σ1) trending NW-SE to NNW-SSE (Fig. 10 a-b). All these structures are consistent with a progressive compression event during Variscan tectonics in the brittle upper crust, after the main folding phase (Sorotchinsky, 1939). These ones are characterized by a strong N- to NW-directed vergence that reflects an overall N-S compression during the main phase of Variscan contraction (Weber 1981), already evidenced by previous thorough microstructural analysis made in the Devonian limestones in and around the Han-sur-Lesse area (Havron et al., 2007; Lacquement, 2001). In terms of deformation timing and kinematics, the brittle structures described here were formed during a compressive event that took place in transition between preliminary extensive tectonics described and quantified by Van Noten et al. (2010; 2012) at the onset of the orogenic

system and the N-S compression that has been identified and documented by several authors (e.g., Delvaux, 1990; 1997; 1998; Lacquement, 2001; Havron et al., 2007).

7. Conclusions and perspectives

Natural caves offer great opportunities to study geological objects, both for the description of geological facies and for the quantification of deformation; with lithologies and geological structures cropping out and being preserved from superficial erosion processes. Digital photogrammetry combined to structure-from-motion algorithm and ground control referencing system is a method applicable to the monitoring, surveying and mapping of geological structures. Acquiring and reconstructing such models in lowlight, complex and confined space such as a cave system is certainly challenging. However, this paper emphasizes its feasibility and describes a workflow to conduct an in-depth geological survey in a karstic environment using a digital outcrop model, from UAV embedded camera and DLSR photographs via SfM photogrammetry techniques. Using these field photographs and the Agisoft Photoscan software, a high resolution digital outcrop model containing more than 395 million points was generated, then georeferenced in the CloudCompare software. This study leads to the 3D mapping and characterization of sedimentary structures. We developed a specific workflow to extract the orientation and spatial distribution of sedimentary beddings and brittle geological structures (faults, slickenlines, joints, tension gashes) exposed on the roof of one of the main chamber of the Lorette cave system which are inaccessible to the fieldworker. Such an approach aims at triggering future applications and new research directions in subsurface environments.

The workflow presented in this study could be used in routine for speleological investigations by providing detailed and accurate morphological mappings and volumetric calculations of cave systems. Constraining the orientation and the exact location of structures such as faults, joints and sedimentary layers is crucial for the understanding of cave morphology and karstological processes (e.g., Delaby, 2001). We hereby demonstrate the strength of using DOM's to perform manual and semi-automatic surveys of the geological structures and then, draw interpretations of structural records in terms of past tectonic regimes and superficial topographical implications.

This has also great implications for paleoseismological studies, which are generally conducted via the observation of fault scarps in trenches. Recent studies have shown the interest of analysing past earthquake-triggered collapse in cave environments (Delaby et al. 2002; Santo et al., 2017; Pérez-Lopez et al., 2017; Camelbeeck et al., 2018). In this context, 3D models can provide a direct quantification of former collapse areas and volumes of

collapsed materials. It also offers perspectives on using such technology as a monitoring tool of active tectonics or recent instabilities. Sudden collapses of natural caves are indeed known to generate a high risk (e.g., Gutierrez et al., 2014; Parise, 2015), especially in urban areas via the formation of sinkholes (Parise and Florea, 2008; Del Prete et al., 2010). Roof collapse is a complex mechanical problematic certainly driven by structural characteristics of the bedrock, such as the fracture intensity, as well as the random variability which affects the mechanical properties of the rock sedimentary pile. Such DOMs in cave chambers, in particular those generating tourism activities or located nearby urbanized areas, should be acquired, listed and analysed for mitigating risks associated with cave collapse.

Other future directions using digital photogrammetry concern the methodological approach. In order to model and obtain a petro-structural survey of complex geological outcrops, the main benefits of digital photogrammetry lie in the spectral information and the high portability of the camera devices. This could be seen as an alternative or complementary approach to LiDAR survey which also tends to become more and more portable (Hosoi et al., 2011; Zlot and Bosse, 2014). The development of fully portable photogrammetry-devoted device combining a source of lighting and camera sensors is indeed crucial to investigate and to easily progress in complex and confined subsurface networks (e.g., lava tubes, former volcanic chambers, inaccessible and irregular cliffs of interest; Thiele et al., 2015; Tavani et al., 2016; Jouve et al., 2017). Such newly developed devices have already been reported in the literature (Jordan, 2017) and are also under development by our side (Watlet et al., 2018).

The spectral information is a second crucial advantage of digital photogrammetry. It allows to contrast and efficiently distinguish superficial spectral signatures in the model that can be accessed via differences in surface state, mineralogical content and/or lithological facies. In this study, such an approach allowed us to detect and spot mineralized veins as well as slickenlines on fault planes and to extract their respective geometries from the roof of the Val d'Enfer chamber (Fig. 8). This also allowed us to determine the nature of the mineral filling within the fault subsets and link fracturation episode to mineralization, a critical source of information for microtectonic analysis (Hancock, 1985) and for mining exploration purposes. Nevertheless, such mineral identification and assemblages' discrimination could be greatly enhanced using multi- or even hyper-spectral sensors that could range from the visible up to infrared spectral bands (e.g., Campbell and Wynne, 2011; Van der Meer et al., 2012 and references therein). Such sensors are already widely used in routine for aerial terrestrial and extra-terrestrial remote sensing but combining large spectral acquisition imaging with digital SfM photogrammetry directly in the field is still in its relatively early stages of development and applicability in geosciences (Minařík and Langhammer, 2016) covering more

archaeological purposes at the moment (Jaillet et al., 2017; Pamart et al., 2017; Uueni et al., 2017). For hydrological purposes too, this could have great implications for the detection and the monitoring of moist zones at the outcrop- but also karstic network-scale following lithologies, opening the door to a better understanding of aquifer recharge and groundwater storage regarding the response/control of the lithostratigraphic pile.

Acknowledgments

We would like to thank all the colleagues who were involved in this project and particularly the ASBL Grottes de Lorette and the municipality of Rochefort for their hospitality and support. We thank Dr. K. Van Noten and another anonymous reviewer for their constructive comments and reviews. We also thank Prof. Dr. C. Passchier for the editorial handling.

References

Abellan, A., Derron, M. H., & Jaboyedoff, M. (2016). “Use of 3D Point Clouds in Geohazards” Special Issue: Current Challenges and Future Trends.

Agisoft LLC, 2015. Agisoft Photoscan Professional [WWW Document]. URL. www.agisoft.com (accessed 16.07.15.)

Allum, J. A. E. (1966). Photogeology and regional mapping. Institute of Geological Sciences, Photogeological Unit.

Angelier, J. (1989). From orientation to magnitudes in paleostress determinations using fault slip data. Journal of structural geology, 11(1-2), 37-50.

Angelier, J. (1994). Fault slip analysis and paleostress reconstruction. Continental deformation, 53-101.

Assali, P., Grussenmeyer, P., Villemin, T., Pollet, N., & Viguier, F. (2014). Surveying and modeling of rock discontinuities by terrestrial laser scanning and photogrammetry: Semi-automatic approaches for linear outcrop inspection. Journal of Structural Geology, 66, 102-114.

Baltsavias, E. P. (1999). A comparison between photogrammetry and laser scanning. ISPRS Journal of photogrammetry and Remote Sensing, 54(2-3), 83-94.

Barchy, L., & Marion, J. M. (2014). Aye-Marche-en-Famenne 54/7-8. Carte géologique de Wallonie-Echelle 1/25.000. Notice explicative.

Bistacchi, A., Griffith, W. A., Smith, S. A., Di Toro, G., Jones, R., & Nielsen, S. (2011). Fault roughness at seismogenic depths from LIDAR and photogrammetric analysis. Pure and Applied Geophysics, 168(12), 2345-2363.

Camelbeeck, T., Quinif, Y., Verheyden, S., Vanneste, K., & Knuts, E. (2018). Earthquakes as collapse precursors at the Han-sur-Lesse Cave in the Belgian Ardennes. Geomorphology, 308, 13-24.

Camelbeeck, T., van Ruymbeke, M., Quinif, Y., Vandycke, S., de Kerchove, E., & Ping, Z. (2012). Observation and interpretation of fault activity in the Rochefort cave (Belgium). Tectonophysics, 581, 48-61.

Campbell, J. B., & Wynne, R. H. (2011). Introduction to remote sensing. *Guilford Press*.

Carrivick, J. L., Smith, M. W., & Quincey, D. J. (2016). Structure from Motion in the Geosciences. John Wiley & Sons.

Chalke, T., Mcgaughey, J., and Perron, G. (2012). 3D software technology for structural interpretation and modeling. Structural Geology and Resources, 56, 16-20.

Chesley, J. T., Leier, A. L., White, S., & Torres, R. (2017). Using unmanned aerial vehicles and structure-from-motion photogrammetry to characterize sedimentary outcrops: An example from the Morrison Formation, Utah, USA. Sedimentary Geology, 354, 1-8.

Corradetti, Tavani, Parente, Iannace, Vinci, Pirmez, Torrieri, Giorgioni, Pignalosa, Mazzoli (2018), Distribution and arrest of vertical through-going joints in a seismic-scale carbonate platform exposure (Sorrento peninsula, Italy): insights from integrating field survey and digital outcrop model. Journal of Structural Geology, Volume 108, March 2018, Pages 121-136.

Del Prete, S., Iovine, G., Parise, M., & Santo, A. (2010). Origin and distribution of different types of sinkholes in the plain areas of Southern Italy. Geodinamica Acta, 23(1-3), 113-127.

Delaby, S., (2001). Paleoseismic investigations in Belgian caves. Geologie en Mijnbouw, 80 (3-4) : 323- 332.

Delaby, S., Vandycke, S., Dejonghe, L., Quinif, Y. et Dubois, Y., (2002). Le système karstique de la Grotte de Hotton (Belgique) : apport de l'étude structurale et cartographique à la karstogenèse et implication paléoseismologique. Aardkundige Mededelingen, 12 : 17- 20.

Delvaux de Fenffe, D. (1985). Géologie et tectonique du Parc de Lesse et Lomme au bord sud du Bassin de Dinant (Rochefort, Belgique). Bull. Soc. Belge Géol., Bruxelles, 94, 81-95.

Delvaux de Fenffe, D., (1990). Structures tardi- et post- hercyniennes dans le bord sud du synclinorium de Dinant, entre Han-sur-Lesse et Beauraing (Belgique). Annales de la Société Géologique de Belgique, 112 (2) : 317-325.

Delvaux de Fenffe, D., (1997). Post-Variscan rightlateral wrench faulting in Ardenne Allochton and the Variscan Front (Belgium). Aardkundige Medelingen, 8: 57-60.

555 Delvaux de Fenffe, D., (1998). Structure and tectonic evolution of the Lesse-et-Lomme
556 region. Spéléochronos hors-série 1998 : 49-51

557 Delvaux, D. (2011). Win-Tensor 3.0. 0 program.

558 Delvaux, D., & Sperner, B. (2003). Stress tensor inversion from fault kinematic indicators
559 and focal mechanism data: the TENSOR program. New insights into structural interpretation
560 and modelling, 212, 75-100.

561 Esposito, G., Mastrorocco, G., Salvini, R., Oliveti, M., & Starita, P. (2017). Application of
562 UAV photogrammetry for the multi-temporal estimation of surface extent and volumetric
563 excavation in the Sa Pigada Bianca open-pit mine, Sardinia, Italy. Environmental Earth
564 Sciences, 76(3), 103.

565 EXIF, Exchangeable image file format. Version 2.3 (2012).
566 http://www.cipa.jp/std/documents/e/DC-008-2012_E.pdf (Accessed 20.12.12)

567 Fonstad, M. A., Dietrich, J. T., Courville, B. C., Jensen, J. L., & Carbonneau, P. E. (2013).
568 Topographic structure from motion: a new development in photogrammetric measurement.
569 Earth Surface Processes and Landforms, 38(4), 421-430.

570 Franceschi, M., Martinelli, M., Gislimberti, L., Rizzi, A., & Massironi, M. (2015). Integration
571 of 3D modeling, aerial LiDAR and photogrammetry to study a synsedimentary structure in the
572 Early Jurassic Calcari Grigi (Southern Alps, Italy). European Journal of Remote Sensing,
573 48(1), 527-539.

574 Gallay, M., Kanuk, J., Hochmuth, Z., Meneely, J. D., Hofierka, J., & Sedlák, V. (2015).
575 Large-scale and high-resolution 3-D cave mapping by terrestrial laser scanning: a case study
576 of the Domica Cave, Slovakia. International Journal of Speleology, 44(3), 277.

577 Girardeau-Montaut, D. (2015). Cloud compare (version 2.9): 3D point cloud and mesh
578 processing software. Open Source Project. EDF R&D, Telecom ParisTech.
579 *http://www.danielgm.net/cc/*

580 Gutiérrez, F., Parise, M., De Waele, J., & Jourde, H. (2014). A review on natural and
581 human-induced geohazards and impacts in karst. Earth-Science Reviews, 138, 61-88.

582 Hancock, P. L. (1985). Brittle microtectonics: principles and practice. Journal of structural
583 geology, 7(3-4), 437-457.

584 Havron, C., Vandycke, S., & Quinif, Y. (2007). Interactivité entre tectonique méso-
585 cénozoïque et dynamique karstique au sein des calcaires dévoniens de la région de Han-
586 sur-Lesse (Ardennes, Belgique). Geologica Belgica, Vol. 10/1-2, pp. 93-108.

587 Hosoi, F., Nakai, Y., & Omasa, K. (2013). 3-D voxel-based solid modeling of a broad-
588 leaved tree for accurate volume estimation using portable scanning lidar. ISPRS Journal of
589 Photogrammetry and Remote Sensing, 82, 41-48.

Jaillet, S., Sadier, B., Hajri, S., Ployon, E., & Delannoy, J. J. (2011). Une analyse 3D de l'endokarst: applications laser-grammétriques sur l'aven d'Orgnac (Ardèche, France). Géomorphologie: relief, processus, environnement, 17(4), 379-394.

Jaillet S., Delannoy J.J, Monney J., Sadier B. (2017) 3-D Modelling in Rock Art Research. Terrestrial Laser Scanning, Photogrammetry, and the Time Factor.The Oxford Handbook of the Archaeology and Anthropology of Rock Art. Edited by Bruno David and Ian J. McNiven. Archaeology, Archaeological Methodology and Techniques. Online Publication Date: Nov 2017 DOI: 10.1093/oxfordhb/9780190607357.013.45

Jordan, Joseph H., (2017), "Modeling Ozark Caves with Structure-from-Motion Photogrammetry: An Assessment of Stand-Alone Photogrammetry for 3-Dimensional Cave Survey". Theses and Dissertations. 2406. *http://scholarworks.uark.edu/etd/2406*

Jouves, J., Viseur, S., Arfib, B., Baudement, C., Camus, H., Collon, P., & Guglielmi, Y. (2017). Speleogenesis, geometry, and topology of caves: A quantitative study of 3D karst conduits. Geomorphology, 298, 86-106.

Lacquement, F. (2001). L'Ardennes Varisque. Déformation progressive d'un prisme sédimentaire préstructuré, de l'affleurement au modèle de chaîne. Société Géologique du Nord, 29, 253 p.

Lague, D., Brodu, N., & Leroux, J. (2013). Accurate 3D comparison of complex topography with terrestrial laser scanner: Application to the Rangitikei canyon (NZ). ISPRS journal of photogrammetry and remote sensing, 82, 10-26.

Lerma, J. L., Navarro, S., Cabrelles, M., & Villaverde, V. (2010). Terrestrial laser scanning and close range photogrammetry for 3D archaeological documentation: the Upper Palaeolithic Cave of Parpalló as a case study. Journal of Archaeological Science, 37(3), 499-507.

Mahmud, K., Mariethoz, G., Baker, A., Treble, P. C., Markowska, M., & McGuire, E. (2016). Estimation of deep infiltration in unsaturated limestone environments using cave lidar and drip count data. Hydrology and Earth System Sciences, 20(1), 359.

Margielewski, W., & Urban, J. (2017). Gravitationally induced non-karst caves: Tectonic and morphological constrains, classification, and dating; Polish Flysch Carpathians case study. Geomorphology, 296, 160-181.

Marion, J.-M., Mottequin, B., Barchy, L., Blockmans, S., Dumoulin, V., (2011). Contexte géologique et structural de la région de Rochefort (Synclinorium de Dinant, Belgique). Geological Survey of Belgium, Profesional Paper 2011, 27–38.

623 Micheletti, N., Chandler, J. H., & Lane, S. N. (2015a). Investigating the geomorphological
624 potential of freely available and accessible structure-from-motion photogrammetry using a
625 smartphone. Earth Surface Processes and Landforms, 40(4), 473-486.
626 Micheletti, N., Chandler, J. H., & Lane, S. N. (2015b). Structure from motion (SFM)
627 photogrammetry. IN: Clarke, L.E. and Nield, J.M. (Eds.) Geomorphological Techniques
628 (Online Edition). London: British Society for Geomorphology. ISSN: 2047-0371, Chap. 2,
629 Sec. 2.2.
630 Michot, P., (1980), Belgique. Introduction à la géologie générale : International Geological
631 Congress, 26th, Paris, Guidebook Gl6, p. 487- 576.
632 Minařík, R., & Langhammer, J. (2016). Use of a multispectral UAV photogrammetry for
633 detection and tracking of forest disturbance dynamics. International Archives of the
634 Photogrammetry, Remote Sensing & Spatial Information Sciences, 41.
635 Niederheiser, R., Mokroš, M., Lange, J., Petschko, H., Prasicek, G., & Elberink, S. O.
636 (2016). Deriving 3d point clouds from terrestrial photographs-comparison of different sensors
637 and software. International Archives of the Photogrammetry, Remote Sensing & Spatial
638 Information Sciences, 41.
639 Mohammed Oludare, I., and Pradhan, B. (2016). A decade of modern cave surveying with
640 terrestrial laser scanning: a review of sensors, method and application development.
641 International Journal of Speleology, 45(1), 8.
642 Pamart, A., Guillon, O., Faraci, S., Gattet, E., Genevois, M., Vallet, J. M., & De Luca, L.
643 (2017). Multispectral photogrammetric data acquisition and processing for wall paintings
644 studies. In ISPRS-International Archives of the Photogrammetry, Remote Sensing and
645 Spatial Information Sciences (Vol. 42, pp. 559-566). Copernicus GmbH.
646 Parise, M. (2015). A procedure for evaluating the susceptibility to natural and
647 anthropogenic sinkholes. Georisk: Assessment and Management of Risk for Engineered
648 Systems and Geohazards, 9(4), 272-285.
649 Parise, M., & Florea, L. J. (2008). I sinkholes nella letteratura scientifica internazionale:
650 una breve rassegna, con particolare riferimento agli Stati Uniti d'America. I fenomeni naturali
651 di sinkhole nelle aree di pianura italiane". Mem. Descr. Carta Geol. d'It, 85, 427-450.
652 Pérez-López, R., Martín-Velázquez, S., Sánchez-Moral, S., Patyniak, M., López-
653 Gutiérrez, J., Cuezva, S., Lario, J., Silva, P.G., Rodriguez-Pascua, M.A. & Giner-Robles, J.
654 L. (2017). New insights on speleoseismology: The geothermal gradient and heat flow values
655 in caves for the study of active faults. Quaternary International, 451, 165-175.
656 Pirson, S., Spagna, P., Baele, J. M., Damblon, F., Gerrienne, P., Vanbrabant, Y., & Yans,
657 J. (2008). An overview of the geology of Belgium. Memoirs of the Geological Survey of
658 Belgium, 55(5), 26.

Quinif, Y., Kaufmann, O., Sagot, D., (2011). Les dépôts de la Grotte de Lorette (Rochefort), in: International symposium “Karst Research Challenges for the XXIst Century” - Brussels, 30 September; Rochefort, 1st October 2011. The Karst Network of the Lomme River, Rochefort Region: Guide Book, Geological Survey of Belgium Professional Paper. Institut royal des Sciences naturelles de Belgique, Service géologique de Belgique, Brussels, pp. 55–63.

Quinif, Y., Van Ruymbeke, M., Camelbeek, T., Vandycke, S., (1997). Les failles actives de la Grotte de Rochefort (Ardenne, Belgique) sont-elles sismogéniques? Installation d’un laboratoire souterrain. Aardkundige mededelingen 8, 153–156.

Remondino, F. (2011). Heritage recording and 3D modeling with photogrammetry and 3D scanning. Remote Sensing, 3(6), 1104-1138.

Remondino, F., Barazzetti, L., Nex, F., Scaioni, M., & Sarazzi, D. (2011). UAV photogrammetry for mapping and 3d modeling–current status and future perspectives. International Archives of the Photogrammetry, Remote Sensing and Spatial Information Sciences, 38(1), C22.

Roncat, A., Dublyansky, Y., Spotl, C., & Dorninger, P. (2011). Full-3d surveying of caves: A case study of marchenhohle (austria). Proceedings of the International Association for Mathematical Geosciences (IAMG 2011).

Salomon, M. L., Grasemann, B., Plan, L., Gier, S., & Schöpfer, M. P. (2018). Seismically-triggered soft-sediment deformation structures close to a major strike-slip fault system in the Eastern Alps (Hirlatz cave, Austria). Journal of Structural Geology.

Santo, A., Budetta, P., Forte, G., Marino, E., & Pignalosa, A. (2017). Karst collapse susceptibility assessment: A case study on the Amalfi Coast (Southern Italy). Geomorphology, 285, 247-259.

Šebela, S., Gosar, A., Košťák, B., & Stemberk, J. (2005). Active tectonic structures in the W part of Slovenia–Setting of micro-deformation monitoring net. Acta Geodyn. Geomater, 2(1), 45-57.

Smith, M. W., Carrivick, J. L., & Quincey, D. J. (2016). Structure from motion photogrammetry in physical geography. Progress in Physical Geography, 40(2), 247-275.

Sorotchinsky, C. (1939). Un accident tectonique eclairant la genese de la salle du Dome dans les grottes de Han. Ann. Soc. Sci. Bruxelles, 97-106.

Tavani, S., Corradetti, A., & Billi, A. (2016). High precision analysis of an embryonic extensional fault-related fold using 3D orthorectified virtual outcrops: The viewpoint importance in structural geology. Journal of Structural Geology, 86, 200-210.

693 Thiele, S. T., Grose, L., Samsu, A., Micklethwaite, S., Vollgger, S. A., and Cruden, A. R.:
694 Rapid, semi-automatic fracture and contact mapping for point clouds, images and
695 geophysical data, Solid Earth Discuss., https://doi.org/10.5194/se-2017-83, in review, 2017.
696 Thiele, S. T., Micklethwaite, S., Bourke, P., Verrall, M., & Kovesi, P. (2015). Insights into
697 the mechanics of en-échelon sigmoidal vein formation using ultra-high resolution
698 photogrammetry and computed tomography. Journal of Structural Geology, 77, 27-44.
699 Triantafyllou, A., Watlet, A., & Bastin, C. (2017). Geolokit: An interactive tool for visualising
700 and exploring geoscientific data in Google Earth. International Journal of Applied Earth
701 Observation and Geoinformation, 62, 39-46.
702 Triantafyllou, A., Watlet, A., Le Mouélic, S. (2018). Sharing Digital Outcrop Models with
703 smartphone-based Virtual Reality. In EGU General Assembly Conference Abstracts (Vol. 20,
704 p. 7370).
705 Uueni, A., Apollonio, F. I., & Hiiop, H. (2017). Photogrammetry and Multispectral Imaging
706 for Conservation Documentation–Tools for Heritage Specialists. In New Activities For
707 Cultural Heritage (pp. 122-130). Springer, Cham.
708 Van der Meer, F. D., Van der Werff, H. M., Van Ruitenbeek, F. J., Hecker, C. A., Bakker,
709 W. H., Noomen, M. F., van der Meijde, M., Carranza, J., de Smeth, J. B., & Woldai, T.
710 (2012). Multi-and hyperspectral geologic remote sensing: A review. International Journal of
711 Applied Earth Observation and Geoinformation, 14(1), 112-128.
712 Van Noten, K., & Sintubin, M. (2010). Linear to non-linear relationship between vein
713 spacing and layer thickness in centimetre-to decimetre-scale siliciclastic multilayers from the
714 High-Ardenne slate belt (Belgium, Germany). Journal of Structural Geology, 32(3), 377-391.
715 Van Noten, K., Van Baelen, H., & Sintubin, M. (2012). The complexity of 3D stress-state
716 changes during compressional tectonic inversion at the onset of orogeny. Geological Society,
717 London, Special Publications, 367(1), 51-69.
718 Vandycke, S., and Quinif, Y. (2001). Recent active faults in Belgian Ardenne revealed in
719 Rochefort Karstic network (Namur province, Belgium). Netherlands Journal of Geosciences,
720 80(3-4), 297-304.
721 Vollgger, S. A., & Cruden, A. R. (2016). Mapping folds and fractures in basement and
722 cover rocks using UAV photogrammetry, Cape Liptrap and Cape Paterson, Victoria,
723 Australia. Journal of Structural Geology, 85, 168-187.
724 Walcors, 2016. http://gnss.wallonie.be/walcors.html, in English (accessed in 2016)
725 Wallace, R. E. (1951). Geometry of shearing stress and relation to faulting. The Journal of
726 Geology, 59(2), 118-130.
727 Watlet, A. (2017), Hydrogeophysical monitoring of groundwater recharge processes
728 through the karst vadose zone at Rochefort (Belgium), PhD thesis, UMONS-ROB.

729 Watlet, A., Kaufmann, O., Triantafyllou, A., Poulain, A., Chambers, J. E., Meldrum, P. I.,
730 Wilkinson, P, Hallet, V., Quinif, Y., Van Ruymbeke, M. & Van Camp, M. (2018). Imaging
731 groundwater infiltration dynamics in the karst vadose zone with long-term ERT monitoring.
732 Hydrology and Earth System Sciences, 22(2), 1563.

733 Watlet, A., Triantafyllou, A., Le Mouélic, S. and Kaufmann, O., (2018). Extracting
734 structural and lithological data from Digital Outcrop Models of cave chambers. In EGU
735 General Assembly Conference Abstracts (Vol. 20, p. 14238-2).

736 Weber, K., (1981). The structural development of the Rheinische Schiefergebirge. Geol.
737 Mijnb. 60, 149–159.

738 Westoby, M. J., Brasington, J., Glasser, N. F., Hambrey, M. J., & Reynolds, J. M. (2012).
739 'Structure-from-Motion'photogrammetry: A low-cost, effective tool for geoscience
740 applications. Geomorphology, 179, 300-314.

741 Wilkinson, M. W., Jones, R. R., Woods, C. E., Gilment, S. R., McCaffrey, K. J. W.,
742 Kokkalas, S., & Long, J. J. (2016). A comparison of terrestrial laser scanning and structure-
743 from-motion photogrammetry as methods for digital outcrop acquisition. Geosphere, 12(6),
744 1865-1880.

745 Willems, L., Ek, C., (2011). Le système karstique de la Lomme. Quelques points
746 d'observation remarquable. Geological Survey of Belgium, Profesional Paper 2011, 3–10.

747 Zlot, R. and Bosse, M. (2014). Three-dimensional mobile mapping of caves. Journal of
748 Cave and Karst Studies, 76(3), 191.

749 Appendices

750 A. Data tables

751 A1. GCP points

752 A2. Triaxes data measurements

753 A3. Structural data measured in the DOM

754

755 B. Supplementary Materials

756 B1. Agisoft photoscan parameters and desktop computer specifications

757 B2. Semi-automatic extraction of strike dip values for each polygons of faulted
758 structures.

759

760 C. Animated view of the Val d'Enfer chamber 3D model (Lorette cave, Rochefort, Belgium)

3-D Digital Outcrop Model for analysis of brittle deformation and lithological mapping (Lorette cave, Belgium)

A. Triantafyllou, A. Watlet, S. Le Mouélic,

T. Camelbeeck, F. Civet, O. Kaufmann, Y. Quinif, S. Vandycke

Figure 1

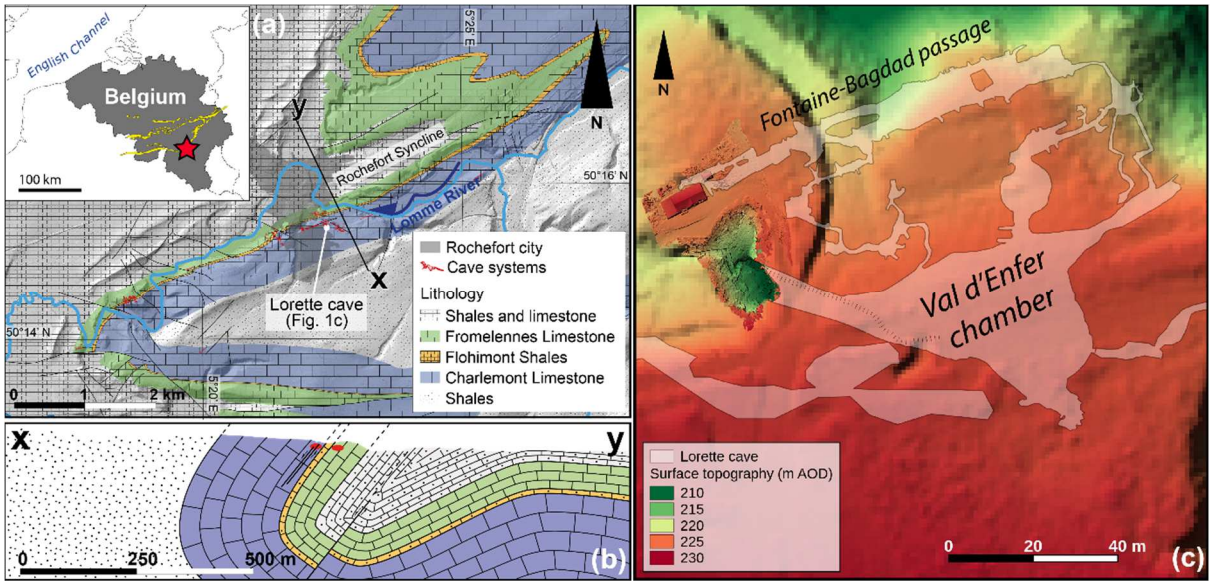

Figure 1. (a) Simplified geological map of the Rochefort area (after Barchy et al., 2014), highlighting limestone formations and the cave networks. (b) Geological cross section (x to y in 1A), modified after Delvaux de Fenffe (1985) displaying an overturned syncline marked by high dipping sedimentary layers (N070–S50) in the Lorette cave area (highlighted in red) and active S-dipping normal faults (Vandycke and Quinif, 2001). (c) General map of the Rochefort Cave Laboratory (RCL in white) overlain on a digital elevation model with a XY resolution of 1m (based on LiDAR data of the Public Service of Wallonia). In the area of the doline giving access to the cave, the DEM is replaced by a high-resolution DEM obtained from a photoscan (Watlet, 2017).

Figure 2

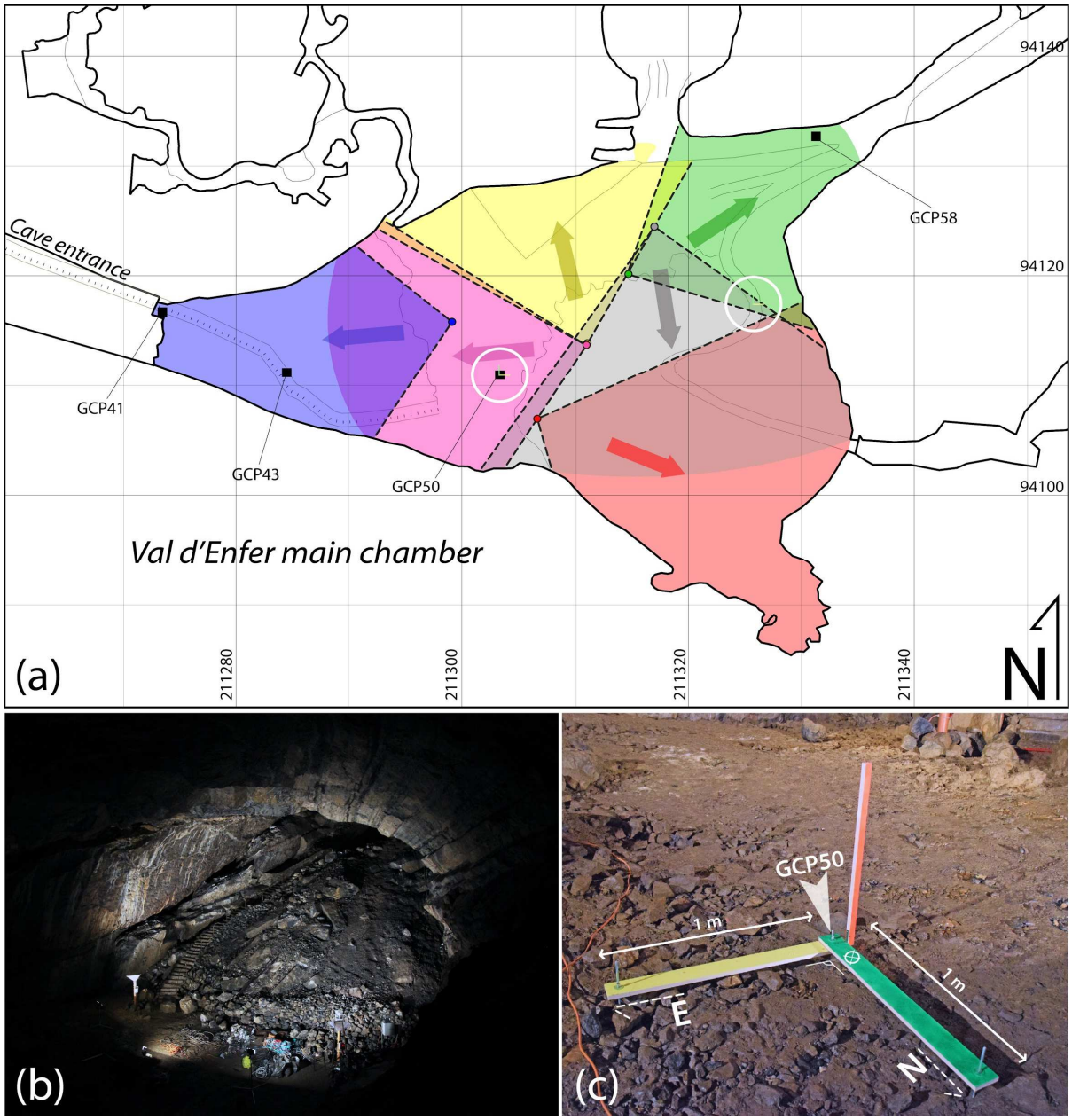

Figure 2 Overview of the field survey in the Val d'Enfer chamber. (a) Sketch map of the Val d'Enfer chamber showing the different chunks made during the survey (random color), the direction of enlightening (colored arrows) and the location of Ground Control Tri-axes (GCT; rounded by white line). (b) Picture showing the enlightening angle for a single chunk (pink chunk here is pointing to the West). (c) Western GCT located on the Ground Control Point 50.

Figure 3

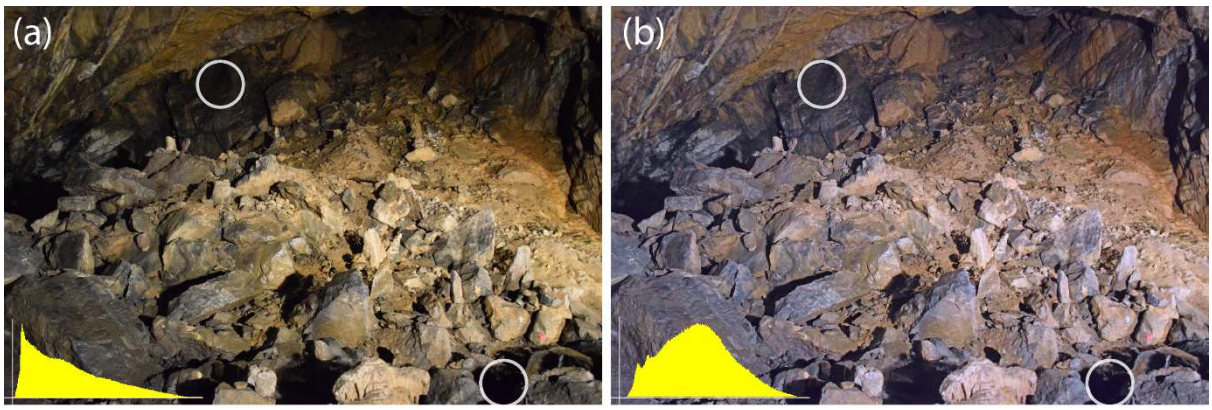

Figure 3. Illustration of a typical preprocessing of a RAW image using a homemade script in Photoshop software. (a) The original photo with its associated mean RGB histogram in yellow. (b) The preprocessed RAW image on which shadows have been highlighted, overexposed pixels have been shadowed and the white balance has been corrected for the yellowish hue of the 3000K halogen spotlight.

30 **Figure 4**

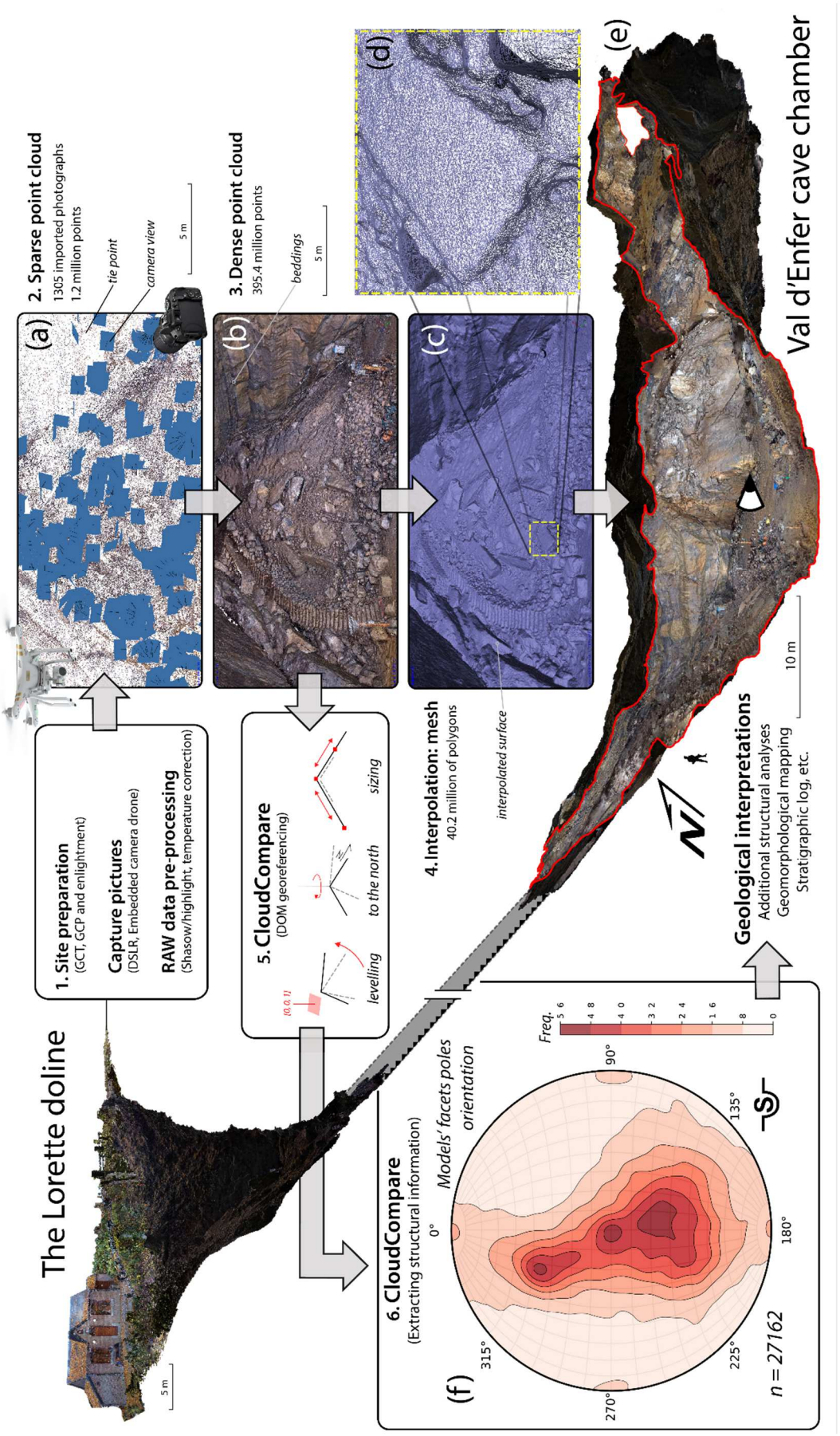

31

Figure 4. Methodological workflow for the generation of the Digital Outcrop Model (DOM). Photographs were acquired both by field and UAV-embedded digital cameras. (a) Alignment procedure of the photographs for determining camera locations and computation of the sparse point cloud. (b) Densification of the sparse point cloud (up to 395.4 million points). (c) Interpolation between each point of the dense point cloud to form a high-resolution mesh. (d) Zoom on the outlined mesh. (e) External view to the NW of the final digital model of the Val d'Enfer chamber and its connection to the surface via the Val d'Enfer doline. (f) Stereonet showing a density contour of the polygons' poles extracted from the raw georeferenced model. A textured version of the 3D model of the main chamber of the Lorette cave can be explored online on the sketchfab repository: *https://skfb.ly/6FQNw*.

Figure 5

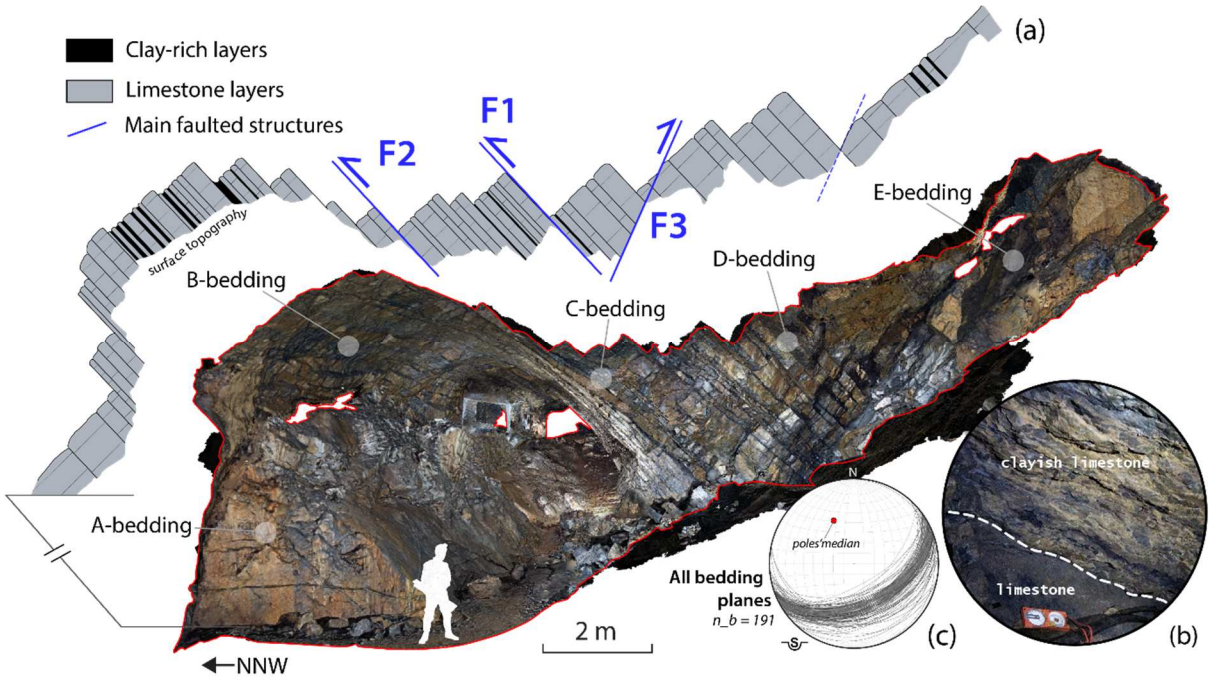

Figure 5. Lithostratigraphic log extracted from the Digital Outcrop Model of the Val d'Enfer chamber. (a) SSE-section of the digital model looking east-wards and detail lithostratigraphic log showing alternating beddings of limestone (grey) and clayish limestones (black level), as controlled and extrapoled from field observations (b). (c) Schmidt stereonet (lower hemisphere) of the sedimentary beddings (*n=191*) attesting a constant strike and dip values of the bedding planes (polar median strike-dip: N065 with 48° dipping to the SE) along the sedimentary pile (from A to E piles, see the manuscript for more details).

Figure 6

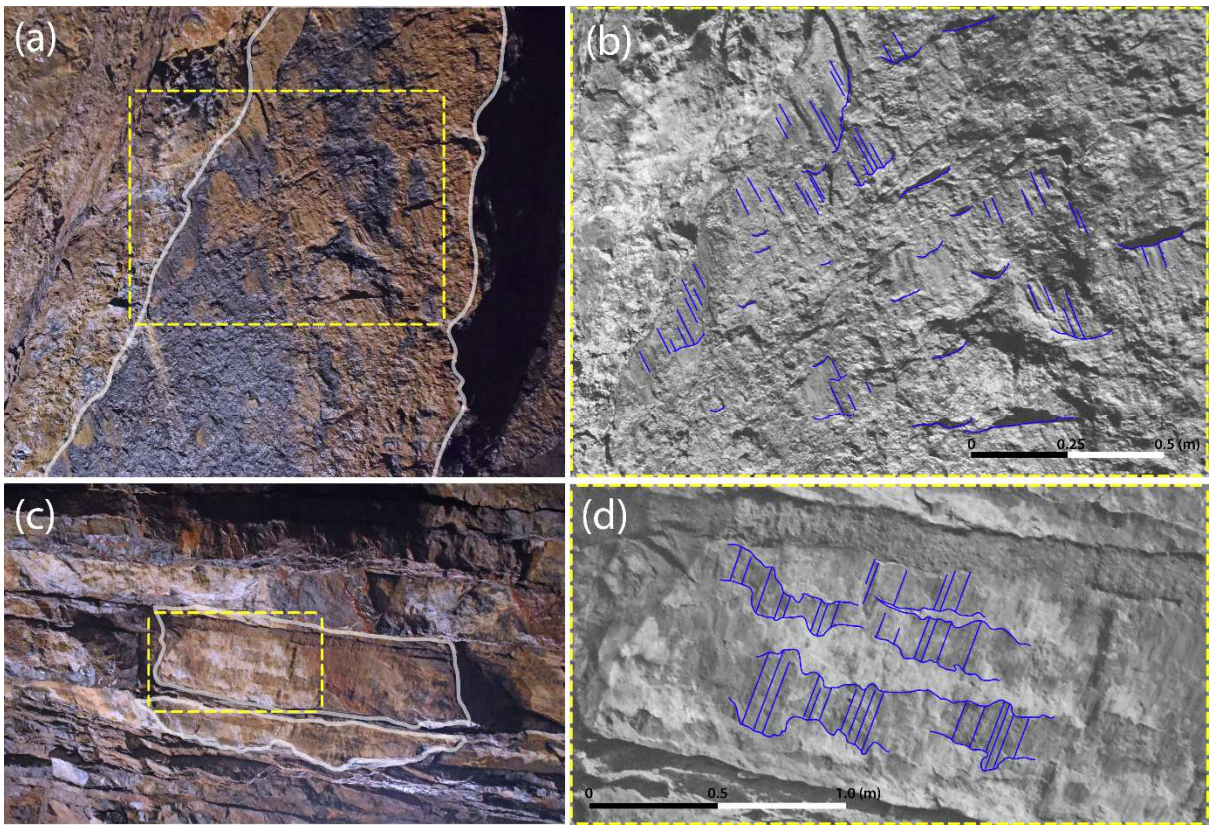

Figure 6. Field photographs showing inaccessible faulted structures forming the roof of the Val d'Enfer chamber (i.e. general view (a) and zoom (b) of fault 5 dipping to the south; general view (c) and zoom (d) of fault 3 dipping to the north; see manuscript for location). Fault surfaces are delimited with the white lines, slickenlines and slickensides are marked by blue lines (original photographs with no marks are shown in the supplementary materials). The surface of F5 is characterized by stylolithic asymmetric micro-scarps and that of F3 by stepping, calcite-filled slickensides. Both fault kinematic criteria show a reverse movement.

Figure 7

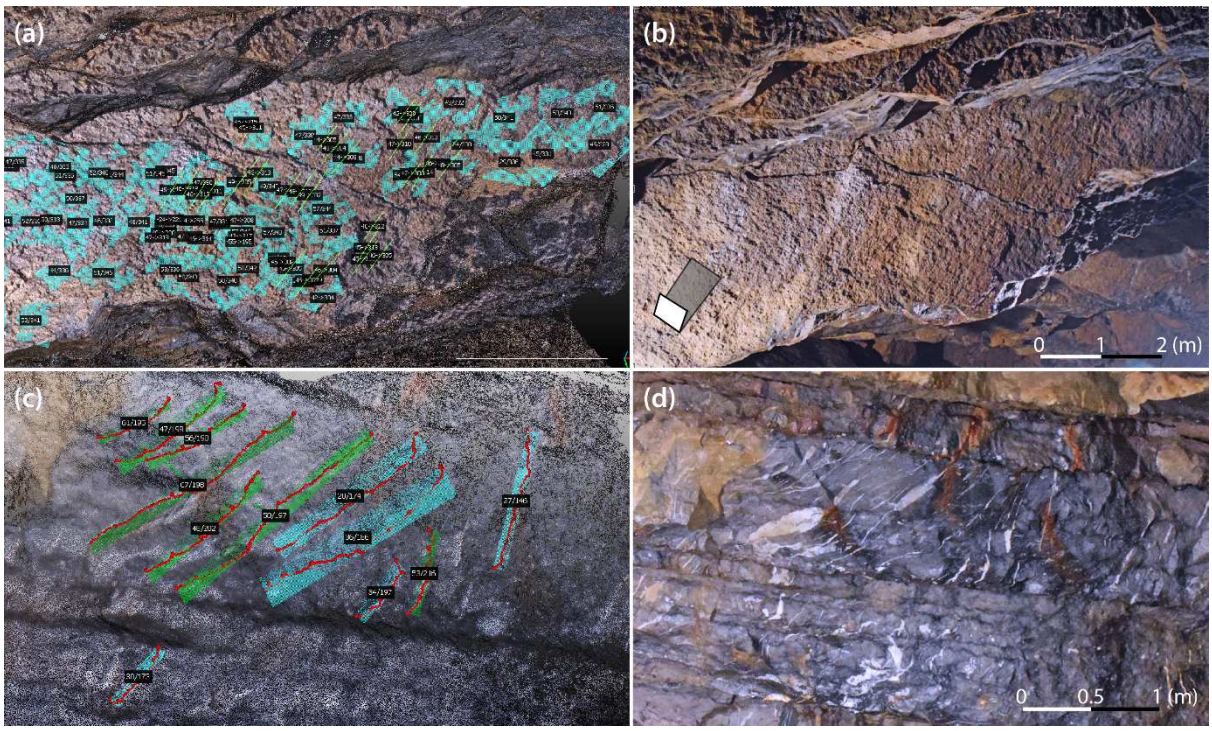

Figure 7. Use of the virtual compass tool in CloudCompare to quantify structures orientations. (a-b) Fault and slickenlines (F2) measured using the direct measurement method for planar structures by averaging the normal vectors included in a virtual circle delimiting the region of interest (see turquoise zones on (a)) and for linear data by tracing a two-point line (see green lines on (a)) lying on the fault plane. The orientation of each measurement is displayed in a black box in CloudCompare (c-d) Calcite-filled planar veins (CJ1_A) measured by tracing the intersection line between the planar structure and the topography of the digital model (red lines on (c)) and computing the best fitting plane (turquoise planes on (c)).

Figure 8

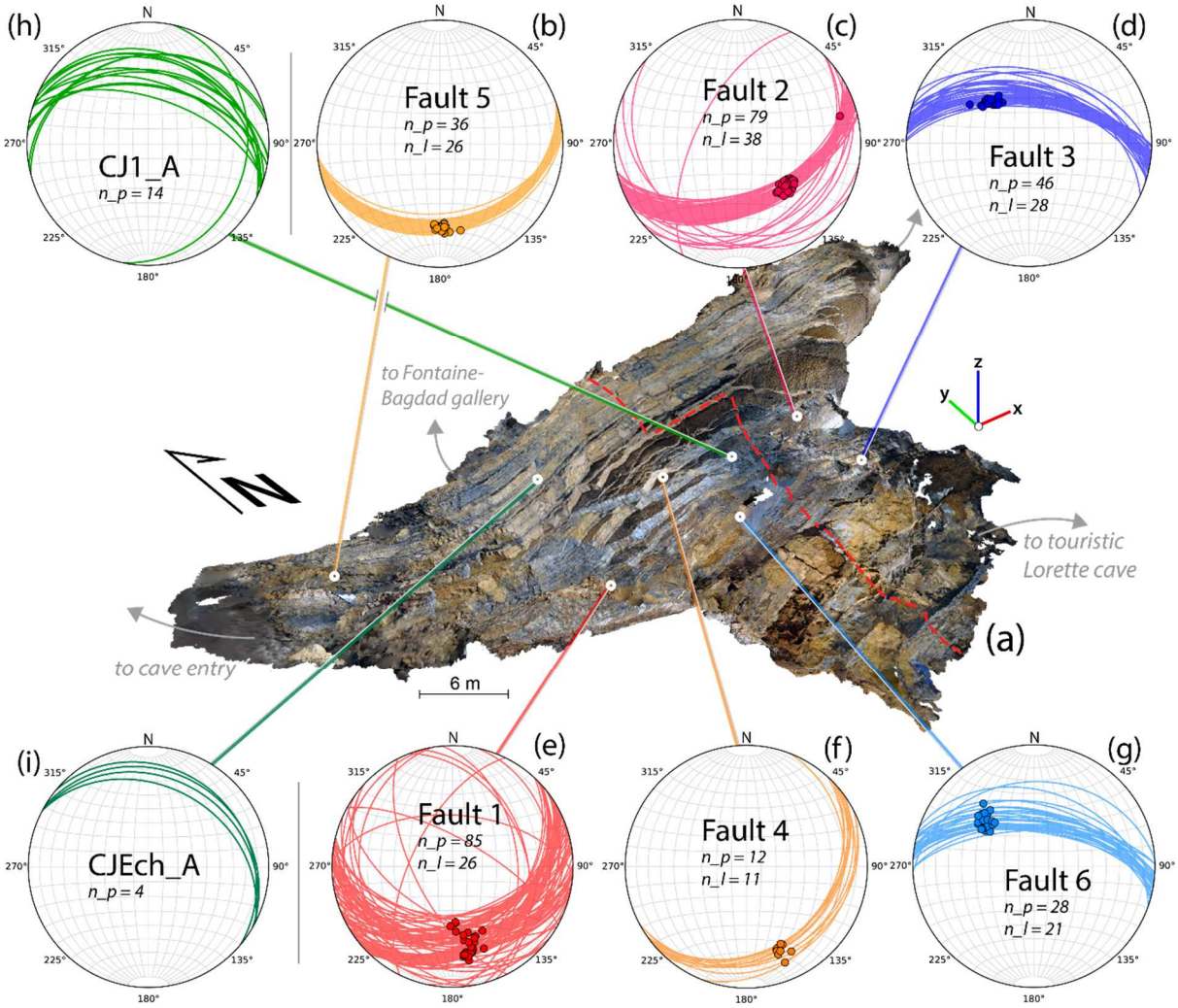

Figure 8. External perspective view (top down, looking to the NE) of the digital model of the Val d'Enfer chamber (a) showing the location of surveyed brittle tectonic structures exposed on the roof of the chamber. Stereonets (b) to (g) display fault-plane and slickenlines orientations measured through a virtual survey. Great circles are for fault planes (*n_p*) and points for slickenlines (*n_l*). Stereonets (h) and (i) display show respectively the orientation of individual calcite-filled planar veins as well as the orientation of planar structures containing the en-echelon calcite-filled veins. All stereonets are drawn on a lower hemisphere Schmidt net using Geolokit software (Triantafyllou et al., 2017).

Figure 9

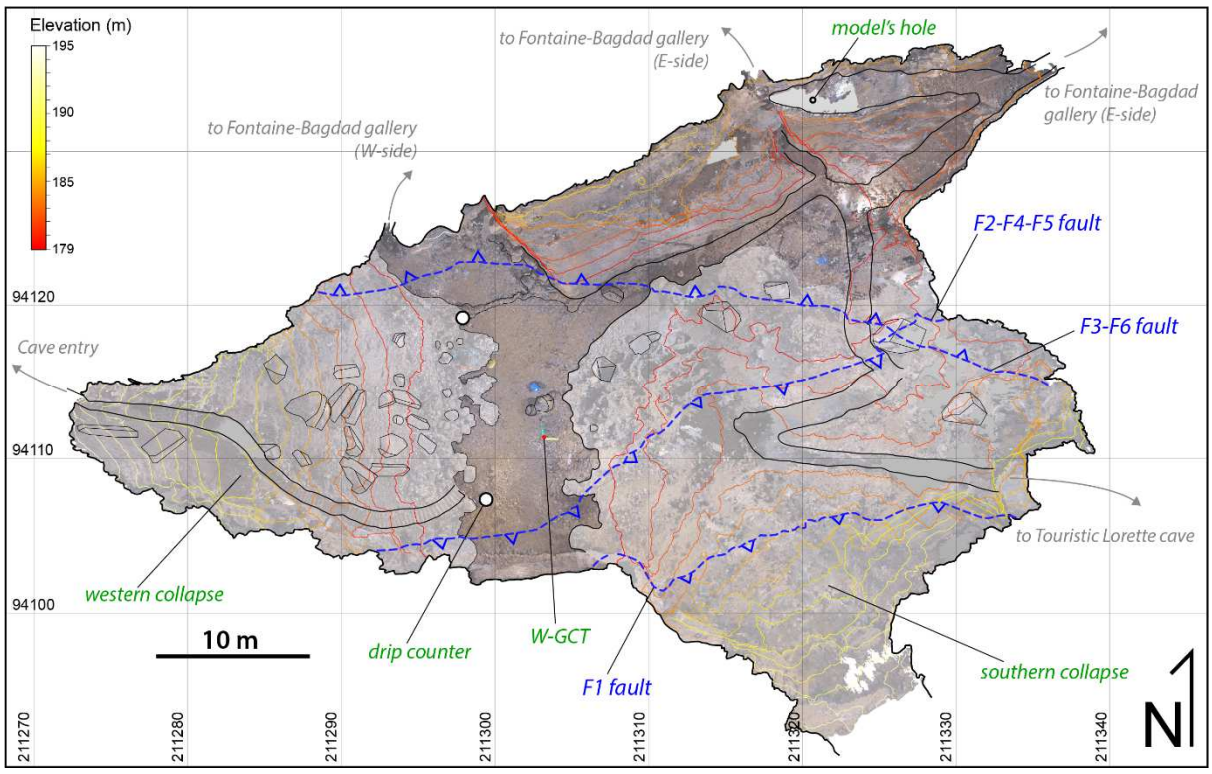

Figure 9. Detailed morphological map of the Val d'Enfer chamber based on the Digital Outcrop Model produced from our study. It shows the two collapse zones (in light white) forming the western and southern elevation of the chamber. The three main faults subsets (F1; F2-F4-F5, F2 and F3-F6) measured on the roof of the chamber have been projected to the cave floor (dashed blue lines) highlighting the probable structural control of karst genesis processes.

Figure 10

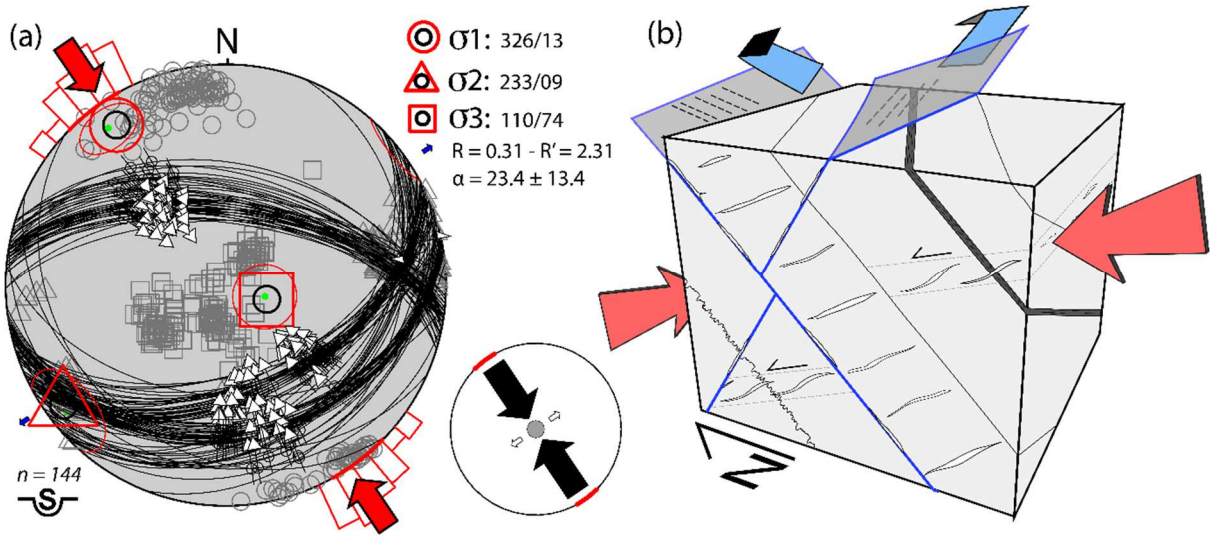

Figure 10. Paleostress analysis of the faults measured 'virtually' in the Val d'Enfer chamber. (a) Stereonet diagram in the stereographic projection (Schmidt lower hemisphere) of measured normal faults (number of planes measurements on faults = 300 and number of linear measurements of slickenlines = 144). Small black arrows represent the slickensides and the direction of relative movement on the fault plane. It shows the main axes of the stress ellipsoid (σ1 ≥ σ2 ≥ σ3) which are respectively displayed as a red circle, triangle and square. The stress tensor was calculated using the Right Dihedra Method, described in Delvaux and Sperner (2003) derived from e.g., Angelier et al. (1994). Fault planes surveyed in the Val d'Enfer chamber recorded a NW-SE to N-S shortening (R: ratio of principal stress differences R = [σ2- σ3 / σ1- σ3]; α: weighted average misfit angle between observed and modelled slip directions). (b) Block diagram summarizing the geometrical relation between brittle structures observed in the Val d'Enfer chamber. Red arrow = σ1.